Computers and Geotechnics 162 (2023) 105656

Contents lists available at ScienceDirect

Computers and Geotechnics

journal homepage: www.elsevier.com/locate/compgeo

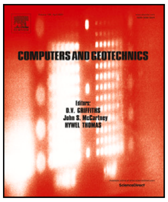

Research paper

Investigation of the load sustaining micro mechanisms of cemented sand using the mesoscale FEM approach

Michail Komodromos [a,*], Mahan Gorji [b], Alexander Düster [b], Jürgen Grabe [a]

[a] *Institute of Geotechnical Engineering and Construction Management, Hamburg University of Technology, Harburger Schloßstraße 36, Hamburg, 21079, Hamburg, Germany*
[b] *Institute for Ship Structural Design and Analysis, Hamburg University of Technology, Am Schwarzenberg Campus 4 C, Hamburg, 21073, Hamburg, Germany*

ARTICLE INFO

Keywords:
Cemented granular material
X-ray CT
Beam hardening
Image adapted meshing technique
Mesoscale FEM

ABSTRACT

While the mechanics of cemented granular material have already been approached by means of constitutive modeling, the capacity of introducing the precise internal structure of multiphase media in numerical simulations offers an alternative perspective of investigation. In specific, means of X-ray computed tomography are able to quantify the internal irregular geometry of the composite material in the form of three-dimensional images. Image analysis can be applied in order to distinguish the topology of each material phase and advanced meshing techniques are able to form a twin meshed domain. The current paper deals with the quantitative description of the morphology of small cemented sand samples, the application of developed image analysis algorithms to treat imaging artefacts (mainly due to beam hardening), the equivalent mesh generation via the image *adapted meshing technique* and the numerical testing using the Finite Element Method. Four samples are imaged, meshed and numerically tested in uniaxial compression; the mesoscale finite element simulations are able to display the intergranular stress transmission chains. A statistical analysis of the load carried by the granular skeleton provides evidence of the influence of the cementation degree and the compaction of the aggregates on the uniformity of the stress distribution.

1. Introduction

Popular in soil enhancement attempts and extensively found in nature, *cemented granular material* (from now on referred to as CGM) is characterized by scientific interest and draws industrial attention. The presence of the binding matrix, such as Portland cement, epoxy, gypsum, calcite, lime, etc. alters the underlying mechanics of the granular medium (Clough et al., 1981; Airey, 1993). In the case of fine Portland cement, which is the basis of the grout mixture used in soil improvement infrastructures, it has been widely stated that the macroscopic mechanical response is determined by the parameters of the percentage of cement content, the grain size distribution, the mineralogy and the relative density (Dano et al., 2004; Zebovitz et al., 1989). Although studies of these macroscopic parameters have provided insight into CGM, it is intuitive to scale down the investigation, in order to understand how do the phase constituents interact. Thanks to the great progress in imaging technology, it has become feasible to capture the exact structure of composite material. Image analysis procedures make possible the segmentation of each individual material phase and advanced meshing algorithms are able to create an equivalent mesh, which reproduces the imaged domain by tetrahedral elements.

This transition from an image to a finite element discretization can be achieved by two different methods; the *non adapted* and the *adapted* meshing technique, called hereafter NAMT and AMT in this section. If the first approach is followed, a non conforming mesh is produced, whose elements that correspond to two different phases are intersected by a material interface (Fig. 1(a)), resulting in a jump of the strain field which could not have been captured by smooth shape functions (Sukumar et al., 2001; Ibrahimbegovic and Melnyk, 2007). Its main advantage is the efficiency of producing equivalent meshes of good element shape, without the need of Delaunay refinement algorithms (Shewchuk, 1970). On the other hand, the AMT reproduces the image morphology by inserting nodes on the material interfaces and placing single material elements on either side (Fig. 1(b)). This approach accurately reproduces the strain jump, thanks to the C^0-continuity of the shape functions and has the capacity of simulating non-linear interface phenomena by introducing zero thickness elements (Park and Paulino, 2011). Still, this discretization process is characterized by relatively greater computational effort on the formation of image based domain, due to the need of Delaunay refinement procedures. In this study, the second method was adopted to ensure

---

* Corresponding author.
E-mail address: michail.komodromos@tuhh.de (M. Komodromos).

https://doi.org/10.1016/j.compgeo.2023.105656
Received 26 February 2023; Received in revised form 23 June 2023; Accepted 8 July 2023

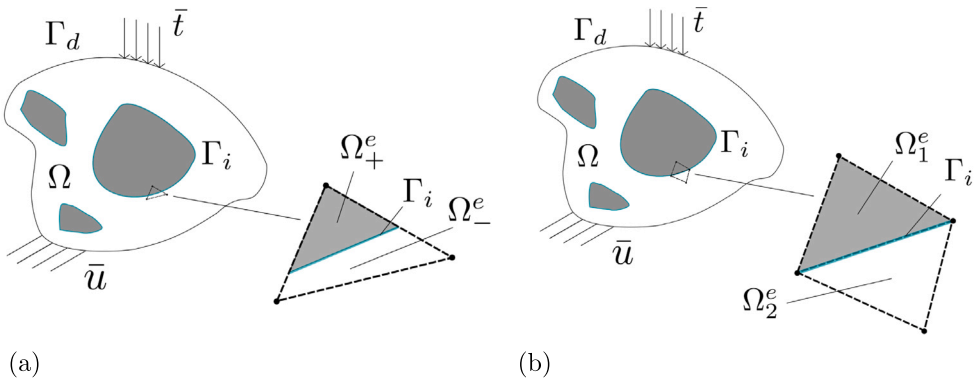

Fig. 1. Incorporation of imaged inclusion in an FE mesh: (a) NAMT (Roubin et al., 2015) (b) AMT.

robust computation of stress localization, i.e. the concentration of large stress magnitudes at limited regions, occurring in CGM either due to material stiffness difference at phase interfaces or mechanical interaction between particles. The formation of a finite element mesh allows for the assignment of boundary conditions and numerical testing of the images that carry the information of the composite internal structure, i.e. the granular fabric, the pore network and the cement matrix.

In the current attempt of investigating the micro mechanics of CGM, four mini samples consisting of coarse to medium-coarse model sand, called *Hamburger Sand*, Milatz (2020) and diluted Portland cement paste, commonly referred to as grout milk (Rosquoët et al., 2003), were scanned by means of X-ray Computed Tomography (X-ray CT) in Laboratoire 3SR, Grenoble, France, see Fig. 2 (a,b,c,d). The production of the small CGM samples was based on a preparation protocol that is established on standard soil mechanics equations and realized by hand mixing. The provision of the basic soil parameters of minimum and maximum void ratio, e_{min} and e_{max}, enables the computation of the available pore space for any relative density value given by the experimentalist. Specifically, this calculation is based on the following standard formulas on soil dry state (Eqs. (1), (2)):

$$e(I_D) = e_{max} - I_D \cdot (e_{max} - e_{min}) \tag{1}$$

$$V_v(e) = \frac{e \cdot V}{1 + e} \tag{2}$$

The notion of the cement saturation degree, S_{cem} describes the amount of pore volume to be occupied by cement mortar and it is dependent on the prescribed relative density. The volume of the cement paste to be added in order to achieve the desired cementation degree is computed by the formula (Eq. (3)):

$$V_{cem} = S_{cem} \cdot V_v \tag{3}$$

In practice, the samples are built in cylindrical Plexiglas molds that are filled in 8 steps; at each step, the weight and volume of the samples is measured and checked if they align with the predictions of the algorithm. In the current study, four samples were produced, under cement saturation degree inputs of 60 and 90% and relative density input of 30 and 70%, from now on referred to as *loose* and *dense*. A study of the radial distribution of cement saturation on the 3D material phase distinguished images confirms that the protocol produced relatively homogeneous samples, with max error of 5% and 10% in the cases of high and low cement saturation correspondingly (see Fig. 3).

The outline of this paper is as follows. In Section 2, the morphological quantification via X-ray CT is described, along with the necessary image correction processes which lead to the phase segmentation. In Section 3, the fundamentals of the image based meshing methods are presented, focusing on the AMT, which is used. In addition, the numerical models are described, i.e. the modeling of the constituent materials, the selection of the boundary conditions and evidence of the objectivity of the results is given. Finally, in Section 4, the numerical stress predictions are presented for the total bulk of the domain, addressing the capacity of FE to capture stress transmission and granting insights into the impact of the cementation degree and the granular compaction on the uniformity of load distribution.

2. Quantification of composite morphology

2.1. X-ray imaging modality and segmentation problem description

Among various imaging means, such as MRI, neutron emission and more, X-ray computed tomography represents one of the dominant scanning modalities used in geomaterials. The X-ray source emits radiation, which penetrates the sample and interacts with the underlying matter, delivering a signal to the X-ray detector, which is ultimately converted to a X-ray attenuation map projection. Essentially, the main property that configures the interaction between the emitted beams and the scanned sample is the density of the last. A finite number of projections at different angles is acquired by rotating and scanning the sample. The reconstruction of the 3D image from the series of projections at different directions is an inverse problem, which can be solved by various methods that are based on the inverse Radon transform. At the current attempt, an algorithm of filtered back projection (Feldkamp et al., 1984), which is analytical inversion of the Radon transform, was used to reconstruct the 3D X-ray attenuation field.

Since the sand model used is characterized by a median grain diameter of 0.68 mm and the cylindrical samples have diameter of 10 mm (2:1 height to diameter ratio), the scale of the problem is defined as the *mesoscale*, where the material heterogeneities are caused by the existing pores and particles. The prefix *meso* refers to the framework where lengths range from hundreds of micrometers to tens of millimeters, in the same manner as the prefices *micro* or *nano* would describe the range of micro/nano meters. The decision over the small dimensions of the samples were made, in order to achieve a resolution of 13 μm per voxel. Such scanning setting is needed to capture information such as the irregular shape of the Hamburger Sand particles and the patches formed by the void filling medium, as shown in similar imaging studies of the same sand material (Milatz et al., 2021).

Still, the interaction between the emitted radiation and the targeted object is a quite complex phenomenon and the derived reconstructed image requires image correction to acquire the morphological information of the material constituents. Despite the fact that the three phases could be easily distinguished by sight in Fig. 2(a,b,c,d), the trinarisation of the 3D images is not trivial due to imaging artefacts, drawing the need for image analysis to clarify the underlying information. In the particular case studied, bias was mainly introduced due to the high density of the materials. When polychromatic X-rays penetrate a relatively dense cylindrical target, such as an assembly of Quartz

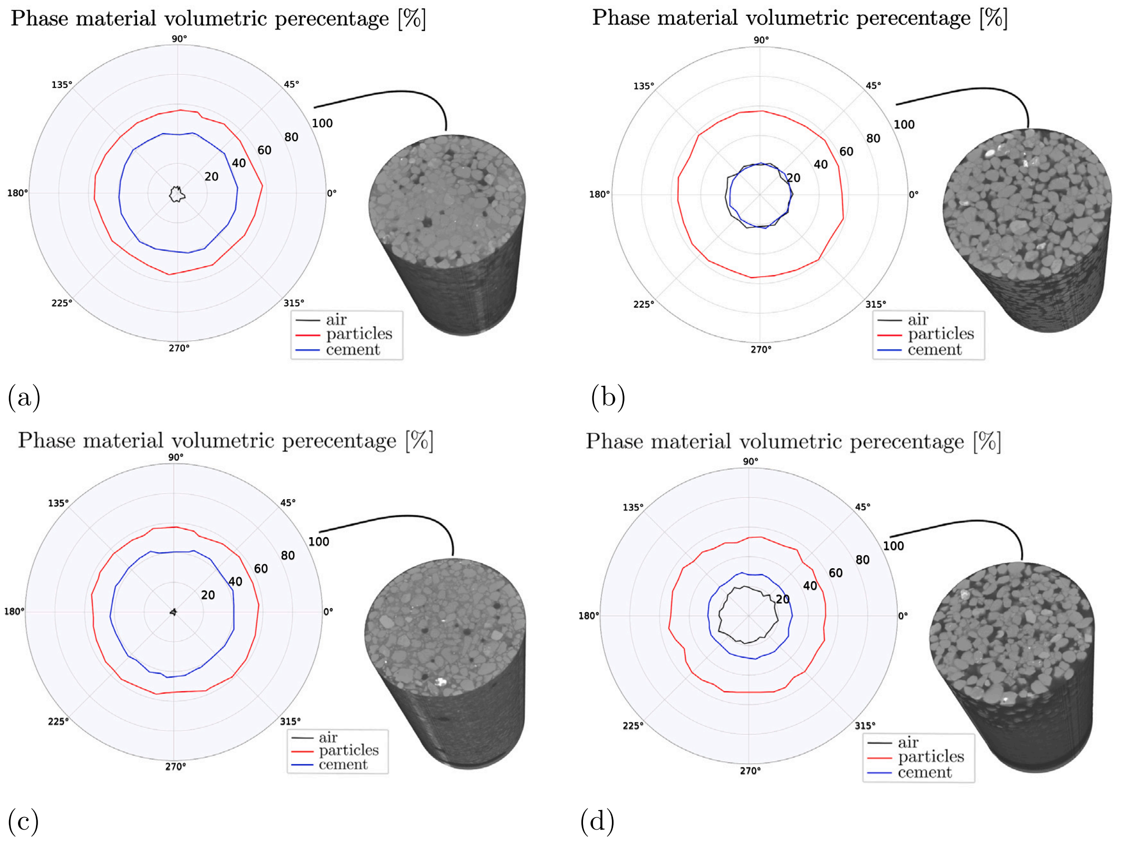

(a)

(b)

(c)

(d)

Fig. 2. Imaged CGM: (a) dense, high saturation, (b) dense, intermediate saturation, (c) loose, high saturation, (d) loose, intermediate saturation.

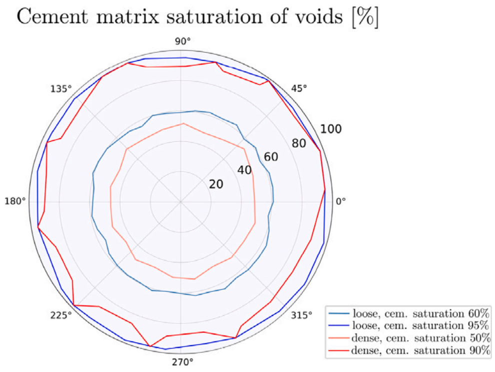

Fig. 3. Radial distribution of cement saturation.

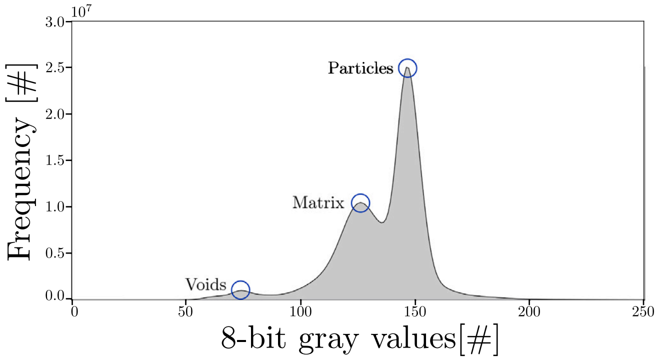

Fig. 4. Form of global histogram.

sand particles, which are bound together by diluted cement mortar, the ‘elongated’ path through the core of the cylindrical sample causes a drop in the energy carried by the photons to the opposite sensor, significantly diverging from the one carried by the beams penetrating the region close to the circumference.

2.2. Against image artefacts

This phenomenon, widely known as *beam hardening*, leads to a gradual gray value drop as moving towards the center of the scanned object, making the distinction of the phases a non-trivial problem (Ketcham and Hanna, 2014). This divergence of gray values corresponding to the same material does not allow to distinguish phases by imposing threshold values, despite the histogram being trimodal (Fig. 4) (Otsu, 1979). The bias causes segmentation problems in the distinction of phases that have close density values (e.g. grains and cement paste), because particle voxels located close to the middle of the cross section have gray values that are close to the ones of cement paste located at the circumference.

To tackle this segmentation problem, an image filter was developed and successfully implemented against beam hardening, calibrating the raw 8-bit gray value map and allowing to distinguish the cement mortar and the Quartz grains with a single threshold value. In the first step, the pore phase is isolated, whose gray value diverges significantly from those corresponding to the cement and the grain phase, as indicated by the broad valley displayed on the global histogram (Fig. 4). Afterwards, the imaged cylinder of cement paste and grains is decomposed into horizontal slices in the axial direction (Fig. 5(a)) and in the second phase in concentric annuli in the radial direction (Fig. 5(b)). At each phase, correction factors are computed based on comparisons between

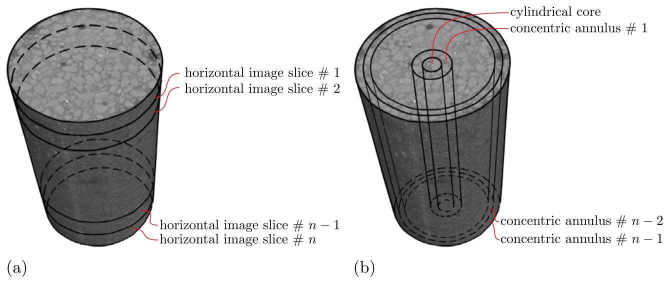

Fig. 5. Image subdomain decomposition: (a) axial direction, (b) radial direction.

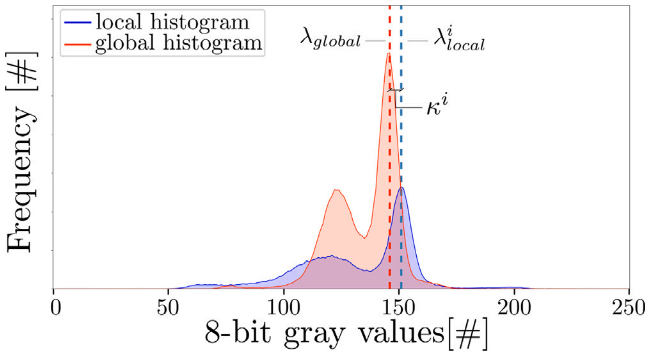

Fig. 6. Global and local histogram comparison.

the local histograms of the subdomains and the global reference histogram of the initial 3D image (Fig. 6). The algorithmic structure of the approach is presented in Algorithm 1.

Essentially, the algorithm divides the image into subdomains and estimates how much they should be uplifted to have an aligned gray value distribution. The correction is quantitatively displayed by drawing the same gray value plot line over the raw and the processed image output (Fig. 7(c)) and it can be visually noticed in Fig. 7(a, b). The plot line of the gray values over the drawn path suggests that all values corresponding to the high attenuation phase (in this case the phase of particles) are lifted to approximately the same level along the whole cross section (Fig. 7(c)).

Algorithm 1 Histogram based gray values alignment

```
Compute the global histogram of the cylindrical domain:    $p_{global}$
Identify the gray value that corresponds to its maximum:
        $\lambda_{global} : p_{global}(\lambda_{global}) = max(p_{global})$
# Axial alignment
For each horizontal image slice i:
    # Gray value alignment procedure
    Compute the local histogram:    $p^i_{local}$
    Identify the gray value that corresponds to its maximum:
        $\lambda^i_{local} : p^i_{local}(\lambda^i_{local}) = max(p^i_{local})$
    Compute the correction factor:
        $\kappa^i = \lambda_{global} - \lambda^i_{local}$
    Add the correction factor to the greyvalues all voxels of slice i:
        $i += \kappa^i$
# Radial alignment
Decompose the cylindrical domain into n - 1 concentric annuli and the core
For each concentric annulus i:
    Repeat the gray value alignment procedure
```

3. Mesoscale simulation framework

3.1. Principles of the image adapted meshing technique

The creation of an equivalent mesh from the phase-segmented image is the main operation to pass the information of the imaged internal structure to a FE model. The result of phase segmentation can be found in Fig. 8(a); each voxel is assigned an integer value according to the material phase it corresponds to. Due to the complexity of the present geometry, such effort requires an efficient meshing scheme. As briefly discussed in the introduction, two main methods can be distinguished: the adapted meshing technique (AMT) and the non-adapted meshing technique (NAMT). The NAMT follows the concept of casting the captured heterogeneities to an unstructured mesh (Roubin et al., 2015; Stamati et al., 2019). To this end, the first step serves to create an unstructured FE mesh that covers the shape and size of the total object to be meshed, without following the geometry of the incorporated heterogeneities (Moës et al., 2003). On the other hand, the image adapted meshing technique (AMT) is based on the reproduction of the image via an FE mesh which is conforming to the imaged material inclusions.

The AMT approach (Boltcheva et al., 2009) was adopted in this study, via a Python wrapper that calls functions from the 3D mesh generation package (Schlömer, 2021) of the open source library CGAL (CGAL, 2022; Alliez et al., 2022). First, the tetranary material image $F : \mathbb{Z}^3 \rightarrow \{0,1,2,3\}$ is decomposed to three binary images $f_i : \mathbb{Z}^3 \rightarrow \{0,1\}, i \in \{1,2,3\}$; all positions of the background, which carry the value 0, are explicitly omitted. Each binary image corresponds to one phase and carries the value of unity for the voxels that topologically correspond to the phase material. A trilinear interpolation scheme is applied to each f_i, which estimates the values at the positions $\boldsymbol{x} \in \mathbb{R}^3$ between the voxels, thus forming continuous functions $\tilde{f}_i : \mathbb{R}^3 \rightarrow \{0,1\}$. An implicit surface description of the boundaries B_i is then derived by applying a levelset at the value of 0.5 on the $\tilde{f}_i$, which provides an implicit surface description of the phase.

Let $E = \{p_0, p_1, \ldots, p_n\}$ be a set of points in $\mathbb{R}^3$ and $Del(E)$ the Delaunay complex of these points. By definition, $Del(E)$ is the geometrical dual of the Voronoi diagram of E, composed of Voronoi cells associated to each point p_i, hereafter called $Vor(p_i)$. $Vor(p_i)$ is a region of $\mathbb{R}^3$ defined by the points that are closer to p_i than any other points in E. The Delaunay complex of E restricted to a volume V, or $Del(E)|V$, is a tetrahedral mesh of elements, whose centers are contained (restricted) inside V. If such procedures take place in the multiple, touching domains $\tilde{f}_i$, the triangular elements which are formed by the touching faces of two tetrahedra of different labels create an air tight envelope surface. From now on, these triangles will be addressed as *facets*.

The iterative discretization of the aforementioned domain (Boissonnat and Oudot, 2005; Pons et al., 2007), as extracted from the segmented image, takes place as follows. Initially, two mesh refinement criteria were provided; the *maximum facet distance*, which serves as the upper limit for the maximum edge length of the triangular facets and the *maximum bulk distance*, which serves as the upper limit for the maximum edge length of the solid tetrahedra. The algorithm starts by sampling small initial point sets $E_{init,i}$ on B_i. Then it computes the formed $Del(E)|V_i$ and the resulting facets. A list of facets and tetrahedra not complying with the given element size criteria is kept. For all of these two and three dimensional elements, refinement points are inserted to reduce their size and maintain their good shapes, based on simplex splitting, as described in detail in Shewchuk (1970). These two refinement processes are combined, with the 2D interface refinement put in priority, and create two sets of points, lying at the material interfaces or the material volumes (Fig. 8(b) and (c) respectively). This procedure terminates at the point when the given criteria are satisfied, thus the lists of non complying elements are empty.

The elements of the AMT approach are sorted in groups that correlate to the corresponding material phase by projecting the center of

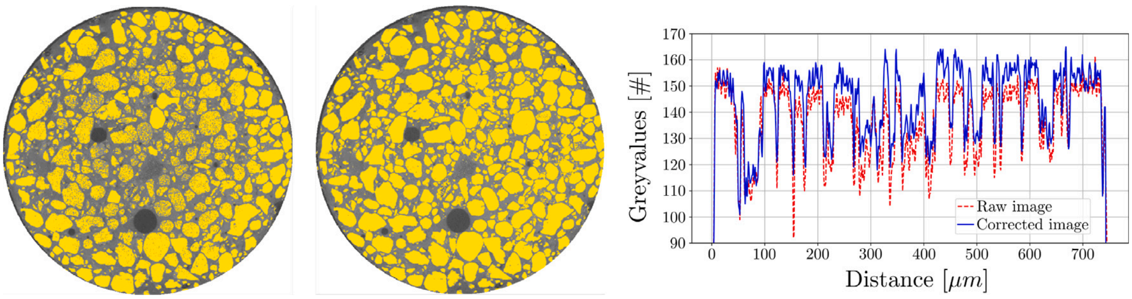

(a) (b) (c)

Fig. 7. Segmentation of aggregates via single value threshold: (a) before filtering, (b) after filtering, (c) gray values regularization.

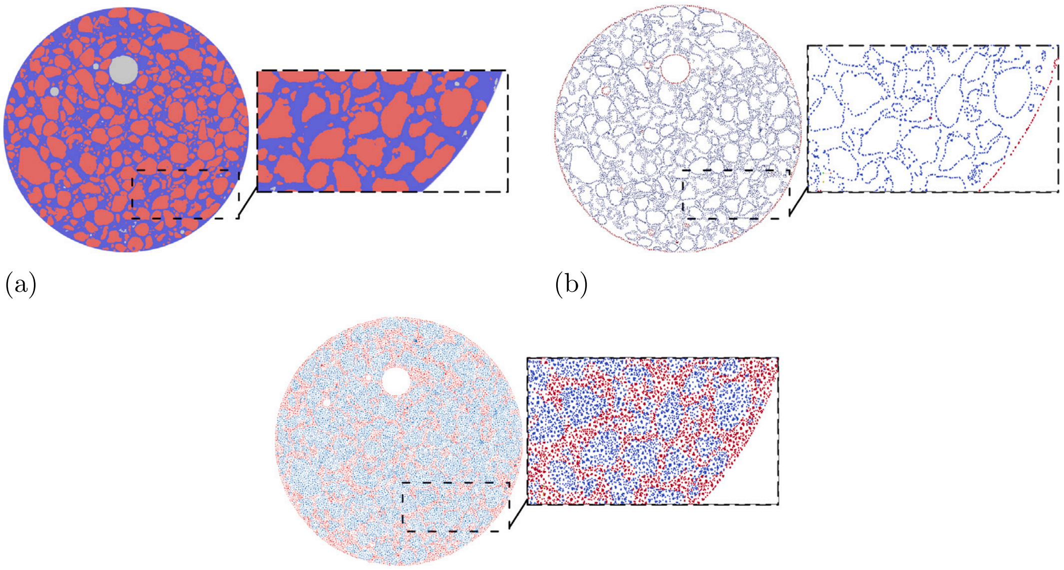

(a) (b)

(c)

Fig. 8. AMT technique: (a) segmented image, (b) interface points, (c) bulk points.

gravity to the value of the matching voxel of the input segmented image (Fig. 9(a, b, c)). The quality of the geometrical representation of the image by the twin mesh was investigated by performing a parametric study of the reproducibility of the loose highly saturated sample image with increased nodal density of the equivalent mesh. The volumes of all phases were calculated in the image by summing the volumes of the voxel of material phase and in the equivalent mesh by summing the volume of the related tetrahedra. The relative error between the volume of the phases between the two representations was calculated, indicating that the error reduces to small values when the mesh is refined (Fig. 10).

3.2. Finite element modeling and numerical verification

This method results into an FE mesh composed of solid tetrahedra elements (*tet4*) on the bulk of the phases and interface triangular elements (*tri3*) on the touching boundaries of these material phases (Fig. 9 (b, c)). Besides the compatibility advantage of being comprehended by standard FE solvers, the AMT as applied in this study provides also the following numerical advantages. First, it is possible to explicitly skip the incorporation of specific phases by commanding the algorithm to avoid placing nodes along domains that carry specific integer values. This practice is applied to the pore network, which is represented by voids, rather than a very soft material. This leads to smaller numbers of DOFs and most important to improved condition numbers of the stiffness matrix. Second, by placing interelement nodes at the material interfaces, the FE method is able to accurately reproduce the strain jumps thanks to the C^0-continuity of the shape functions, therefore avoiding the need of introducing any enrichment function (Joulaian and Düster, 2013; Düster and Allix, 2020). For the sake of simplicity, all interface *tri3* are removed, establishing a perfect bond between the different materials, under the assumption of no detachment or slippage.

The outcome of the aforementioned pre-processing approach was modified to serve as an input configuration file to be imported in a FE-code, which in the present case is the implicit finite element program Abaqus Standard (Smith, 2009), developed and distributed by Dassault Systèmes. The choice of this mesh based approach, instead of a mesh free one, such as the Discrete Element Method (Cundall and Strack, 1971) was made due to the following reason. In cases of highly cemented granular material, the irreversible motion of grains, which is macroscopically addressed as plasticity, is restrained by the binding mortar and the contact fabric does not radically change during external loading. The existing phases of cement mortar and sand particles are interacting, deformable solids. Although the granular skeleton remains the stiffer phase, thus the arrangement of grains primarily shapes the distribution of stresses, the cement mortar remains a mechanically active component, able to aid the stress transmission. This consideration about the solid material components led to the hypothesis that the load distribution mainly relies on the deformation of the solid constituents. In order to capture precisely the strains exhibited by the cement matrix

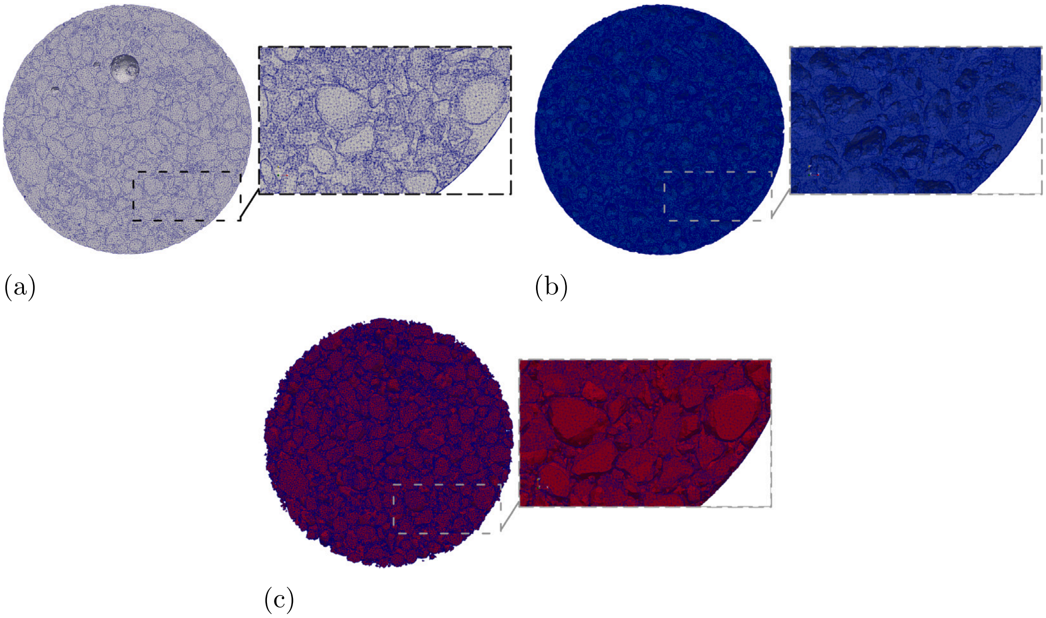

Fig. 9. AMT technique: (a) unsorted mesh, (b) cement mortar phase, (c) particle phase.

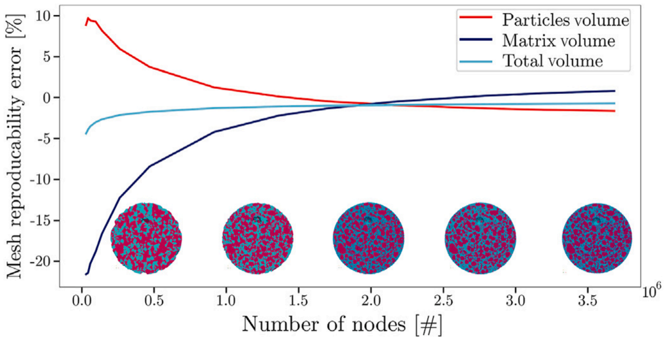

Fig. 10. Reproducibility study between reference image and generated meshes.

and the incorporated particles, the Finite Element Method was chosen. Its continuum based approach (Zienkiewicz et al., 2014) is able to capture and predict accurately developing stress localization. It is worth mentioning that such method would probably not function well for the case of non-cemented granular assemblies, where re-arrangement of the particles and large deformations on the macro-scale occur.

The current FE model is solely based on linear elasticity; the CGMs are treated as trinary composite materials (Fig. 11), instead of assemblies of bonded particles. Specifically, the granular skeleton is considered to be a deformable continuum, rather than a composition of individual rigid bodies which obey the laws of motion and interact via point contact. In the same spirit, the mortar matrix is considered to be a deformable body which interacts with the granular skeleton via fixed interfaces. Finally, the pore network is completely excluded by the domain, replaced by stress free element surfaces. This concept suits CGM as the binder restricts the rearrangement of grains until the post failure strain levels, thus the form and shape of the phases is maintained. Even at post failure levels, the mechanical response is dictated by fracturing phenomena, such as matrix cracking and grain crushing, which also require prediction of stress distributions. A unit displacement of 1 μm is prescribed on the top face of the domain to reveal the stress distribution of the initial and assumed constant forms of the composites at different saturation degrees and granular compactions. For the mechanical characterization of the granular phase, a common set of linear elastic material properties was assigned, assuming that all grains roughly consist of the same Quartz material, which was mechanically tested and addressed to have an overall stiffness in the order of some GPa, see Wichtmann and Triantafyllidis (2014). As far as the diluted mortar is concerned, it was assigned a set of elastic parameters some order of magnitudes smaller than the Quartz particles, similarly by assuming homogeneity. In order to avoid singularities in the system, caused by rigid body motion or insufficient boundary conditions, tangential lateral displacement restrictions have been applied on four nodes lying on the circumference of the cylinder (Fig. 11). These kinematic restrictions suppress rigid body motion without causing any parasitic stresses.

Still, the simulation requires verification, since the mesh density can strongly influence the deformation mode of the system, thus the accuracy of the numerical results. The characteristic effects of this pathogenesis are excessive stiffness and a weakness of accurately displaying the underlying physics. In order to quantify mesh dependency, a parametric study was conducted to observe the macroscopic response of the domain for increasing discretization densities. For the sake of economy, the scalar equivalents of one-dimensional spring stiffness and volumetric strain were chosen as representative magnitudes of the response of the models. Evidently, the addition of nodes results into reduced stiffness and increased volumetric contraction. According to the parametric analysis on Fig. 12(a, b) the response of the domains will ultimately tend to a plateau. Because of the high computational costs accompanied by the increased nodal density, the discretization was carried out up to 3.3 million nodes.

4. Load sustaining mechanisms on the particle scale

On the particle scale, the full-field load bearing mechanisms were studied according to the axial stress distribution given by the FE simulations. The contours show that the load is mainly transmitted via intergranular contact, along with narrow stress bridges formed at the close cement mortar, highlight with red color tones at Fig. 13(a, b, c). Considering the locations of the load transmission itself and the orientation of the stress chains, the interpretation of the results according to granular micro-mechanics suggests the following. Thanks to the continuum framework of FEM, the propagation of the stress chains can also be tracked inside the granular volume. The form of these chains displays high localization on the contact edges, followed by dissipation over the bulk, which depends on the size and the

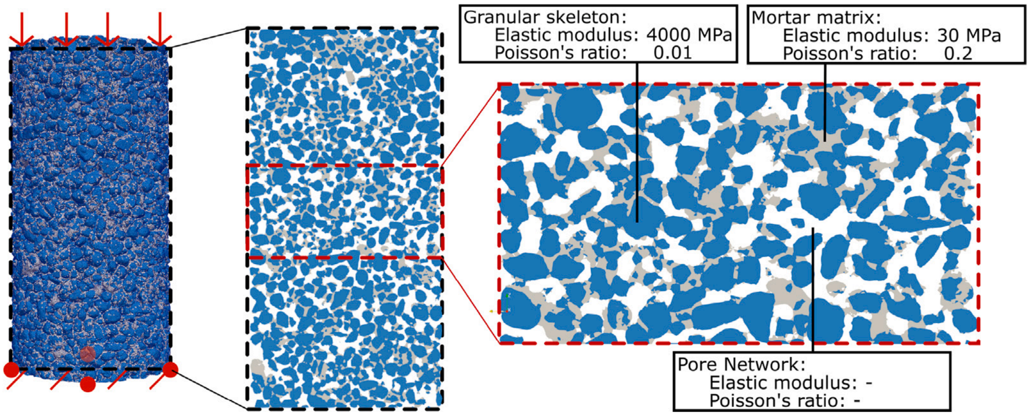

Fig. 11. Uniaxial compression numerical testing.

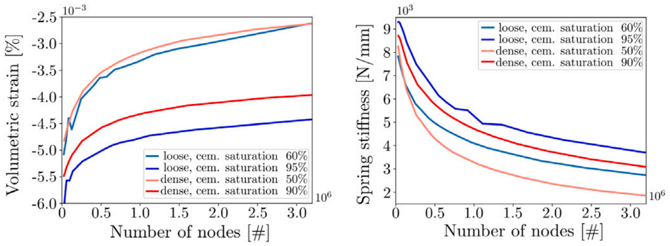

(a) (b)

Fig. 12. Mesh dependency study: (a) macroscopic contraction, (b) macroscopic stiffness.

shape of the particles. It is worth mentioning that the shape of this stress predictions looks quite similar to the strain output provided by experiments utilizing photoelasticity (Sanvitale et al., 2022); the stress paths present alignment with the loading direction, passing through the bulk of the particles.

According to the numerical results, the shape orientation seems to show the following property. If the particle shape is aligned to the direction of the load, then the whole bulk is effectively mobilized to carry the stress. If not, the grain still carries the stress, as defined by its contact points, but a significant volume of the particle remains unloaded, due to the divergence of orientation between its granular body and the loading direction. Out of the total global network, which is defined by the granular fabric, the subgroup of the contacts that are aligned to the load direction is activated, additionally mobilizing the neighboring cement matrix. As far as the cement fabric is concerned, its morphology seems also to be important and correlated with the direction of loading. In the same spirit as the granular fabric, if the cement patches and bridges between the particles are aligned to the load direction (Fig. 13(a, b, c)) the material carries the load more effectively, which in the case of linear elastic simulations is interpreted by a stiffer and less dilatant macroscopic response. It can be concluded that the response of the CGM is mainly a matter of the orientation of the meso-structure. Thus, denser granular packing and greater cement mortar presence results into a 'richer' contact network, which probably leads to an increased number of contacts aligned to the load direction, therefore increased number of stress paths, thus greater capacity of granular skeleton mobilization.

In order to quantify the influence of the cementation degree and the granular compaction, the following post-processing scheme is developed. Initially, the granular skeleton of the original image are particle-labeled using the watershed algorithm (Beare and Lehmann, 2006), meaning that all voxels corresponding to the same particle are assigned a unique value, as shown in Fig. 14(a). Then each tetrahedron of the granular skeleton (Fig. 14(b)) is correlated to its corresponding particle. Ultimately, the axial stress average over every individual grain is sorted and the statistical analysis of the results leads to following conclusions. First, CGM are rather heterogeneous composites, no matter how densely they are compacted or how cemented saturated they are. Indicatively, in all studied cases, 80% of the grains carry less than 12% of the max particle averaged axial stress (Fig. 15(a)). Still, the trends suggest that the distribution becomes more uniform as the packing gets denser. Furthermore, increased cementation seems to facilitate the distribution over highly loaded grains (Fig. 15(b)). This evidence is in agreement with the aforementioned idea, suggesting that cementation and densification allows for extended stress distribution via particle contact and/or transmission through stress bridges over the cement mortar.

5. Conclusions

This work demonstrated the practice of mesoscale FE analysis on four imaged CGM samples, aiming to investigate the evolving load sustaining mechanisms on the grain scale. The meso structure was quantified in form of gray scale 3D images via means of X-ray CT. In order to distinguish the constituent material phases, the images were corrected against artefacts, mainly caused by beam hardening phenomena. The applied filter conducted gray value alignment on the axial and radial direction, based on histogram comparison of cylindrical subdomains. This phase segmentation process was followed by the conversion of the images into tetrahedral FE meshes, based on the open source CGAL library. This conversion technique was tested by performing parametric studies; it was shown that the produced meshes displayed adequate morphological reproducibility and that mesh refinement supports convergence of quantities such as macroscopic stiffness or contraction.

The mesoscale FE response presented the stress transmission chains on the mesoscale, which was mainly carried out by intergranular contact. The full field output suggested that the loading activates the subgroup of contacts which are aligned to the loading direction. In addition, the orientation of the particles seems to influence their effective contribution to the stress bearing. Finally, a statistical analysis confirmed that CGMs are highly heterogeneous and the uniformity of the stress distribution is primarily affected by the granular packing and secondarily by the cementation degree.

The progression of this research attempt will aim on improving the numerical scheme and investigating the anisotropy of CGMs. Effort on prediction of fracturing phenomena, by implementing the XFEM (Belytschko and Black, 1999; Moës et al., 1999) scheme combined with an LEFM framework (Griffith, 1921; Irwin, 1958) will be conducted. The aim is the capture of failure triggering phenomena of matrix cracking and grain crushing, whose blend defines the failure of the

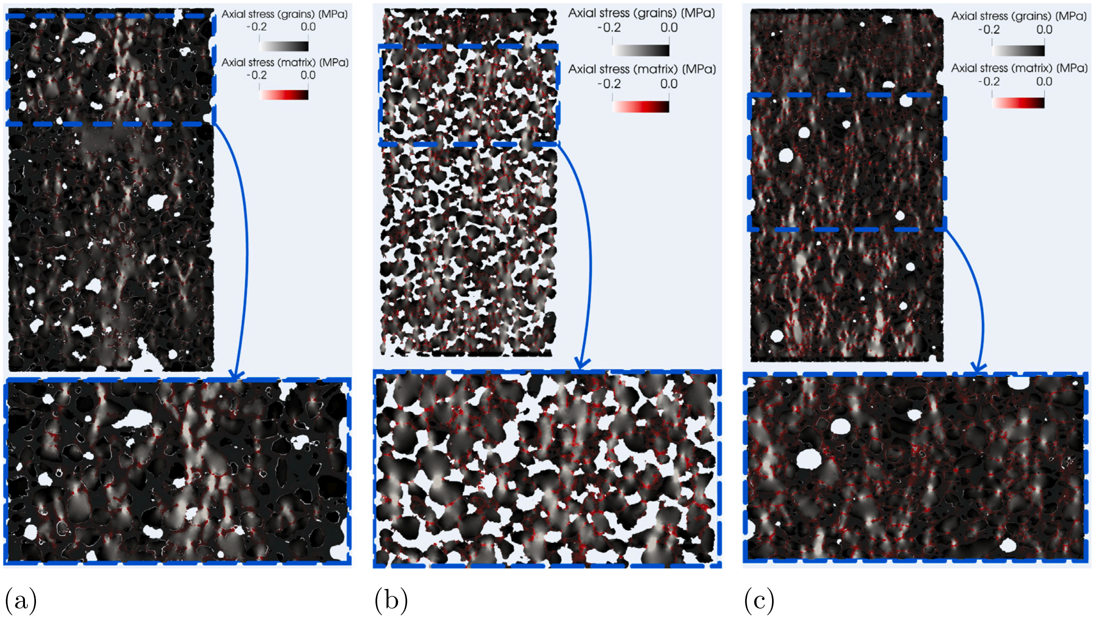

Fig. 13. Axial stress distribution: (a) dense, high saturated CGM, (b) dense, low saturated CGM, (c) loose, high saturated CGM.

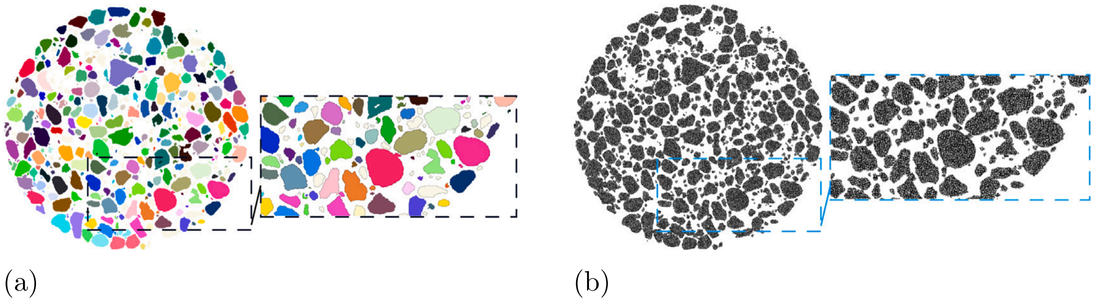

Fig. 14. FE result projection on the individual particles: (a) particle labeled granular skeleton, (b) FE mesh.

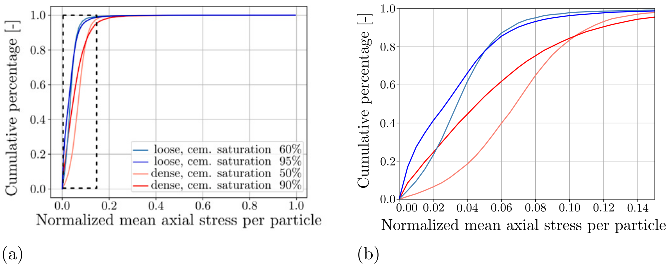

Fig. 15. Statistical output of the particles loading: (a) total, (b) detail.

CGM (Tengattini et al., 2014; Das et al., 2014). A safe prediction of this phenomena may provide evidence on the mechanisms triggering them, along with their influence on the load re-distribution on the fractured material. As far as anisotropy is concerned, REV numerical testing under different directions is planned, in order to investigate how is anisotropy influenced by the contact network.

CRediT authorship contribution statement

Michail Komodromos: Methodology, Investigation, Software, Visualization, Writing – original draft. **Mahan Gorji:** Writing – review & editing. **Alexander Düster:** Writing – review & editing, Supervision. **Jürgen Grabe:** Supervision.

Declaration of competing interest

The authors declare that they have no conflict of interest.

Data availability

Data will be made available on request.

Acknowledgments

The authors are grateful for the beam time provided by Laboratoire 3SR, Grenoble, France and would like to thank Pascal Charrier and Olga Stamati for their help in X-ray scanning procedure.

Funding

The authors gratefully acknowledge the financial support provided by the DFG (Deutsche Forschungsgemeinschaft) under the grant number GR 1024/41-1 and DU 405/17-1.

References

Airey, D.W., 1993. Triaxial testing of naturally cemented carbonate soil. J. Geotech. Eng. 119 (9), 1379–1398. http://dx.doi.org/10.1061/(ASCE)0733-9410(1993)119:9(1379).

Alliez, P., Jamin, C., Rineau, L., Tayeb, S., Tournois, J., Yvinec, M., 2022. 3D mesh generation. In: CGAL User and Reference Manual, 5.5.1 ed. CGAL Editorial Board.

Beare, R., Lehmann, G., 2006. The watershed transform in ITK-discussion and new developments. Insight J. http://dx.doi.org/10.54294/lf8u75.

Belytschko, T., Black, T., 1999. Elastic crack growth in finite elements. Internat. J. Numer. Methods Engrg. 45, 601–620.

Boissonnat, J.D., Oudot, S.Y., 2005. Provably good sampling and meshing of surfaces. Graph. Models 67, 405–451, hal-00488829.

Boltcheva, D., Yvinec, M., Boissonnat, J.D., 2009. Feature preserving Delaunay mesh generation from 3D multi-material images. Comput. Graph. Forum 28, 1455–1464. http://dx.doi.org/10.1111/j.1467-8659.2009.01522.x.

CGAL, 2022. CGAL User and Reference Manual. CGAL Editorial Board, s.l..

Clough, W., Sitar, N., Bachus, R., 1981. Cemented sands under static loading. J. Geotech. Eng. Div. 107, 799–817. http://dx.doi.org/10.1061/AJGEB6.0001152.

Cundall, P.A., Strack, Q.D.L., 1971. A discrete numerical model for granular assemblies. Geotechnique 29, 47–65.

Dano, C., Hicher, P.Y., Tailliez, S., 2004. Engineering properties of grouted sands. J. Geotech. Geoenviron. Eng. 130 (3), 328–338. http://dx.doi.org/10.1061/(ASCE)1090-0241(2004)130:3(3289).

Das, A., Tengattini, A., Nguyen, G., Viggiani, G., Hall, S., Einav, I., 2014. A thermomechanical constitutive model for cemented granular materials with quantifiable internal variables. Part II - Validation and localization analysis. J. Mech. Phys. Solids http://dx.doi.org/10.1016/j.jmps.2014.05.

Düster, A., Allix, O., 2020. Selective enrichment of moment fitting and application to cut finite elements and cells. Comput. Mech. 65, http://dx.doi.org/10.1007/s00466-019-01776-2.

Feldkamp, L., Davis, L.C., Kress, J., 1984. Practical cone-beam algorithm. J. Opt. Soc. Amer. A 1, 612–619.

Griffith, A., 1921. The phenomena of rupture and flow in solids. Phil. Trans. R. Soc. A 221, 163–198.

Ibrahimbegovic, A., Melnyk, S., 2007. Embedded discontinuity finite element method for modeling of localized failure in heterogeneous materials with structured mesh: An alternative to extended finite element method. Comput. Mech. 40, 149–155. http://dx.doi.org/10.1007/s00466-006-0091-4.

Irwin, G.R., 1958. Fracture, Elasticity and Plasticity. Springer, Berlin.

Joulaian, M., Düster, A., 2013. Local enrichment of the finite cell method for problems with material interfaces. Comput. Mech. 52, http://dx.doi.org/10.1007/s00466-013-0853-8.

Ketcham, R.A., Hanna, R.D., 2014. Beam hardening correction for X-ray computed tomography of heterogeneous natural materials. Comput. Geosci. (ISSN: 0098-3004) 67, 49–61. http://dx.doi.org/10.1016/j.cageo.2014.03.003.

Milatz, M., 2020. An automated testing device for continuous measurement of the hysteretic water retention curve of granular media. Acta Geotech. 15, http://dx.doi.org/10.1007/s11440-020-00922-y.

Milatz, M., Hüsener, N., Andò, E., Viggiani, G., Grabe, J., 2021. Quantitative 3D imaging of partially saturated granular materials under uniaxial compression. Acta Geotech. 16, http://dx.doi.org/10.1007/s11440-021-01315-5.

Moës, N., Cloirec, M., Cartraud, P., Remacle, J.F., 2003. A computational approach to handle complex microstructure geometries. Comput. Methods Appl. Mech. Engrg. (ISSN: 0045-7825) 192 (28–30), 3163–3177. http://dx.doi.org/10.1016/S0045-7825(03)00346-3.

Moës, N., Dolbow, J., Belytschko, T., 1999. A finite elemet method for crack growth without remeshing. Int. J. Numer. Method Eng. 46, 131–150.

Otsu, N., 1979. A threshold selection method from gray-level histograms. IEEE Trans. Syst. Man Cybern. 9 (1), 62–66. http://dx.doi.org/10.1109/TSMC.1979.4310076.

Park, K., Paulino, G., 2011. Cohesive zone models: A critical review of traction-separation relationships across fracture surfaces. Appl. Mech. Rev. 64, 1002. http://dx.doi.org/10.1115/1.4023110.

Pons, J.P., Ségonne, F., Boissonnat, J.D., Rineau, L., Yvinec, M., Keriven, R., 2007. High-quality consistent meshing of multi-label datasets. In: Karssemeijer, N., Lelieveldt, B. (Eds.), Information Processing in Medical Imaging. IPMI 2007. In: Lecture Notes in Computer Science, vol. 4584, Springer, Berlin, Heidelberg, http://dx.doi.org/10.1007/978-3-540-73273-0-17.

Rosquoët, F., Alexis, A., Abdelhafid, K., Phelipot, A., 2003. Experimental study of cement grout: Rheological behavior and sedimentation. Cem. Concr. Res. 713–722.

Roubin, E., Vallade, A., Benkemoun, N., Colliat, J.B., 2015. Multi-scale failure of heterogeneous materials: A double kinematics enhancement for Embedded Finite Element Method. Int. J. Solids Struct. 52, http://dx.doi.org/10.1016/j.ijsolstr.2014.10.00122.

Sanvitale, N., Gheller, C., Bowman, E., 2022. Deep learning assisted particle identification in photoelastic images of granular flows. Granul. Matter 24, 65. http://dx.doi.org/10.1007/s10035-022-01222-w.

Schlömer, N., 2021. pygalmesh: Python interface for CGAL's meshing tools. http://dx.doi.org/10.5281/zenodo.5564818.

Shewchuk, J., 1970. Tetrahedral mesh generation by delaunay refinement. In: Proc. 14th Annu. ACM Sympos. Comput. Geom.. http://dx.doi.org/10.1145/276884.276894.

Smith, M., 2009. ABAQUS/Standard User's Manual, Version 6.9. Dassault Systèmes Simulia Corp., United States.

Stamati, O., Roubin, E., Andò, E., 2019. Tensile failure of micro-concrete: from mechanical tests to FE meso-model with the help of X-ray tomography. Meccanica 54, 707–722. http://dx.doi.org/10.1007/s11012-018-0917-0.

Sukumar, N., Chopp, D.L., Moës, N., Belytschko, T., 2001. Modeling holes and inclusions by level sets in the extended finite-element method. Comput. Methods Appl. Mech. Engrg. (ISSN: 0045-7825) 190 (46–47), 6183–6200. http://dx.doi.org/10.1016/S0045-7825(01)00215-8.

Tengattini, A., Das, A., Nguyen, G.D., Viggiani, G., Hall, S.A., Einav, I., 2014. A thermomechanical constitutive model for cemented granular materials with quantifiable internal variables. Part I—Theory. J. Mech. Phys. Solids 70, 281–296. http://dx.doi.org/10.1016/j.jmps.2014.05.02.

Wichtmann, T., Triantafyllidis, T., 2014. Stiffness and damping of clean quartz sand with various grain-size distribution curves. J. Geotech. Geoenviron. Eng. 140, http://dx.doi.org/10.1061/(ASCE)GT.1943-5606.0000977.

Zebovitz, S., Krizek, R.J., Atmatzidis, D.K., 1989. Injection of fine sands with very fine cement grout. J. Geotech. Eng. 115 (12), 1717–1733. http://dx.doi.org/10.1061/(ASCE)0733-9410(1989)115:12(1717).

Zienkiewicz, O.C., Taylor, R.L., Fox, D., 2014. The Finite Element Method for Solid and Structural Mechanics. Butterworth-Heinemann, Oxford.